Electromagnetic modeling of terahertz quantum cascade laser waveguides and resonators

Stephen Kohen, Benjamin S. Williams, and Qing Hu
Department of Electrical Engineering and Computer Science and Research Laboratory of Electronics, Massachusetts Institute of Technology, Cambridge, Massachusetts 02139

Finite-element numerical modeling and analysis of electromagnetic waveguides and resonators used in terahertz quantum cascade lasers are presented. Both metal-metal and semi-insulating (SI) surface-plasmon ridge waveguide geometries were investigated. Simulations and analysis of two types were performed: two-dimensional waveguides (eigenmode calculation), and two- and three-dimensional resonators (facet reflectivity calculation for infinite width and finite width waveguides, respectively). Waveguide simulations extend previous transverse one-dimensional analyses to two dimensions (for the lateral and transverse dimensions), and quantify the breakdown of the one-dimensional approximation as the ridge width is reduced. Resonator simulations in two and three dimensions are presented and are used to obtain facet reflectivities and output radiation patterns. For the metal-metal waveguide structures, these resonator simulations quantitatively show strong deviations for terahertz facet reflectivities from those predicted by the effective index method. However, the effective index method for calculating reflectivities is shown to still be valid for SI surface-plasmon waveguides. © *2005 American Institute of Physics*.
[DOI: 10.1063/1.1855394]

I. INTRODUCTION

The recent development of terahertz (THz) quantum cascade lasers (QCLs) demonstrates their considerable potential as a compact source of coherent radiation for bridging the so-called "terahertz gap."[1–3] The terahertz frequency range (1–10 THz, 30–300 μm) exists between the microwave and infrared regimes, and has long been identified to have wide-ranging applications in spectroscopy, imaging, and remote sensing. However, largely due to a lack of compact, cheap, and convenient continuous-wave (cw) terahertz sources, this frequency range has so far been underdeveloped.

The design of optical confinement structures was a key development in the extension of QCLs from the midinfrared regime to longer wavelengths. This was due, in part, to the difficulty in scaling the dimensions of conventional dielectric waveguides up with increasing wavelength as well as the increase in free-carrier loss ($\alpha_{fc} \propto \lambda^2$) that occurs in the semiconductor cladding and active regions. To date, two types of waveguides, both of which use the surface plasmon as the confinement mechanism, have enabled terahertz laser operation: the semi-insulating (SI) surface-plasmon waveguide[1–3] and the metal-metal waveguide[4,5] (see Fig. 1). In the SI surface-plasmon waveguide, the mode is composed of surface plasmons attached to the upper metal contact and a thin semiconductor layer grown just below the active region that is highly doped to act as a so-called plasma layer (Re$\{\epsilon\}$ <0). The plasma layer also serves as an electrical path between the side metal contacts and the active region. Although the mode extends substantially into the SI substrate, the overlap with doped regions is small so that the free-carrier loss is small. The second type of waveguide, known as the metal-metal waveguide, is similar in form to a microstrip transmission line where confinement is obtained between metal layers directly above and below the active region. While this waveguide is expected to display relatively low loss and a high confinement factor, its fabrication requires a more complicated wafer bonding and substrate removal process.[4]

Proper resonator design remains an important factor in efforts to extend terahertz QCL operation beyond cryogenic operation and to even longer wavelengths. In this paper, we compare the absorptive losses, optical confinement factor, and facet reflectivity for these two waveguide structures using two- and three-dimensional electromagnetic finite-element calculations.[6]

For the design of the resonator (composed of waveguide and mirrors) we use as a figure-of-merit the threshold gain g_{th} as given by the condition
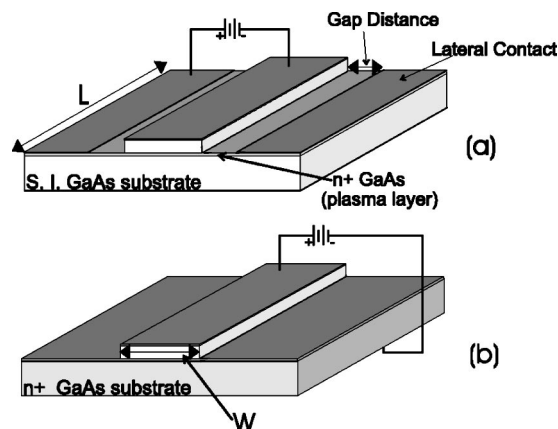

FIG. 1. Schematics of (a) SI surface-plasmon and (b) metal-metal waveguide structures.

$$g_{th} = \frac{\alpha}{\Gamma} = \frac{\alpha_w + \alpha_m}{\Gamma}. \tag{1}$$

Here α, the total loss, includes absorptive losses contributed by the waveguide α_w and coupling losses due to the mirrors α_m; Γ is the confinement factor. All the parameters on the right side of Eq. (1) are determined by the passive waveguide structure, while the material gain on the left side of Eq. (1) is determined by the transport and radiative properties of the quantum-well gain medium. Minimizing the threshold gain results in reduced threshold current densities and increased operating temperatures.

Previous design simulations of terahertz QCLs, based on one-dimensional slab waveguide techniques,[4] focused solely on the confinement in the transverse (epitaxial growth) direction, from which α_w and Γ were obtained. The use of such a one-dimensional approximation is appropriate when the lateral waveguide dimension is much larger than the wavelength in the semiconductor. The simulations reported in this paper extend previous one-dimensional analyses of both SI surface-plasmon and metal-metal waveguides to two dimensions to quantitatively take into account effects of certain two-dimensional design variables beyond the scope of one-dimensional analysis. For SI surface-plasmon waveguides, the effects of the plasma layer's doping and thickness, the waveguide width, the substrate thickness, and the gap distance between the side metal contacts and the waveguide are analyzed. For metal-metal waveguides, the effects of waveguide width and thickness are analyzed.

In addition, previous design simulations calculated mirror loss (i.e., facet reflectivity) using the effective index method, the same method used in optical and midinfrared waveguide designs from which terahertz QCLs evolved. This method states that the reflection coefficient is simply the Fresnel reflection coefficient,[7] which is determined solely by the effective material refractive index. For a GaAs/air interface, this gives facet reflectivities of $R \sim 0.32$, depending on the propagation constant of the lasing mode.[1,8] Mirror loss, given by $\alpha_m = -\ln R/L$, where L is the cavity length, therefore was solely a function of cavity length. Although this method is still successfully used for midinfrared QCL design,[9] in the microwave regime, waveguides are designed using transmission line theory, and reflectivities are determined using the impedance mismatch method. Radiation from an open-ended waveguide is treated using an antenna impedance, which is computed numerically.[10] The computations carried out for this paper offer a numerical solution to the problem of determining terahertz facet reflectivities. Resonator simulations for metal-metal waveguides in two and three dimensions and for SI surface-plasmon waveguides in two dimensions are presented and analyzed.

The frequency range investigated for this paper is 1–7 THz, which is below the *Reststrahlen* band ($\omega_{TO}/2\pi \approx 8$ THz) in GaAs where phonon losses are not prohibitively high for the operation of terahertz QCLs. Above the Reststrahlen band lies the midinfrared regimes, which use a combination of surface-plasmon and conventional dielectric waveguides. Results are only displayed for the frequency range of 1–5 THz, since the threshold gain α/Γ is lower in the higher frequency range of 5–7 THz for both the SI surface plasmon and the metal-metal waveguide structures.

II. WAVEGUIDE ANALYSIS

Waveguide analysis gives numerical estimates of the propagation constants and confinement factors for selected eigenmodes of a specified waveguide. The power loss is given by $\alpha_w = 2 \, \text{Im}\{\beta\}$, where β is the propagation constant of the mode $\phi(x,y)e^{i\beta z}$. Terahertz waveguide losses are mainly due to free-carrier loss in the metal and doped semiconductor and phonon absorption loss in the semiconductor. The latter is only significant for frequencies near the Reststrahlen band (>5 THz for GaAs) at elevated temperatures. To simplify matters, phonon loss is not included in these simulations, but given the fact that the modes for these waveguides are largely confined to the semiconductor, phonon losses can simply be added on to the calculated α_w. Free-carrier loss was taken into account by using an effective complex permittivity following the Drude–Lorentz approximation:

$$\epsilon(\omega) = \epsilon_{core}(\omega) + i \frac{ne^2\tau}{\omega m^*(1 - i\omega\tau)}, \tag{2}$$

where, for these simulations, $\epsilon_{core}(\omega)$ was set at $12.96\epsilon_0$ for GaAs and did not include phonon effects. The Drude relaxation times used in this paper were 0.1 ps for the highly doped GaAs layers, 0.5 ps for the lightly doped GaAs layers (active region), and 0.06 ps for the Au contacts. In addition, the carrier densities were set at 2×10^{15} cm^{-3}, 5×10^{18} cm^{-3}, and 5.9×10^{22} cm^{-3} for the active region, injector layer, and metal layers for all simulated devices. The active region doping level is at the lower end of the values used in present terahertz QCL devices and represents a best-case scenario for minimization of free-carrier loss. This becomes important at lower frequencies where free-carrier loss in the active region itself will predominate over that from the cladding. Although we use the bulk Drude model to describe free-carrier loss absorption in the multiple quantum-well active region, it is expected to be a reasonable approximation at frequencies greater than those of the intersubband resonances in the injector region.[11] More importantly, its use allows quantitative comparison of competing waveguide designs where free-carrier losses in the active region cannot be neglected.

For simplicity, all waveguides simulated have vertical side walls that can be fabricated using dry etching. In addition, for all calculations of the mirror loss, $\alpha_m = -\ln R/L$, L was chosen to be set at 3 mm and reflectivity values for R are taken from calculated results given in the resonator section of this paper.

A. SI surface-plasmon waveguides

The SI surface-plasmon waveguide [Fig. 1(a)] simulated for this paper consists of a 10 μm thick (except 15 μm thick at 2.0 THz) active region layer sandwiched between a 100 nm thick contact layer doped at $n = 5 \times 10^{18}$ cm^{-3} with a Au contact on top, and, on the bottom, an n$^+$ GaAs layer referred to as the plasma layer doped with a carrier concen-
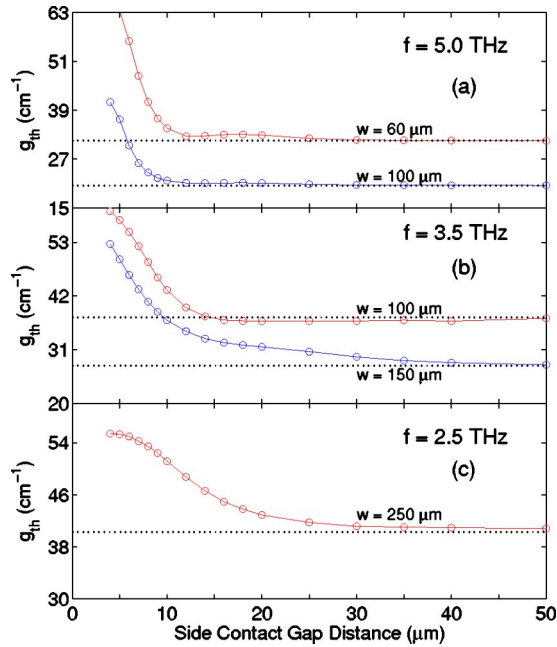
FIG. 2. (Color online) SI surface-plasmon waveguide two-dimensional (2D) simulation results for the threshold gain vs side contact gap distance: (a) f =5 THz with a plasma layer thickness of 0.3 μm doped at 3×10^{18} cm^{-3}, (b) f=3.5 THz with a plasma layer thickness of 0.4 μm doped at 1.5 $\times 10^{18}$ cm^{-3}, and (c) f=2.5 THz with a plasma layer thickness of 0.6 μm doped at 1×10^{18} cm^{-3}. Waveguide widths are noted in each case. Dotted lines show convergence to the waveguide's threshold gainwithout any side contacts.

tration of n_{pl}. These layers are grown on a 200 μm thick (except where noted) undoped GaAs substrate, with a bottom metal layer contact. Metal layers were set to be 400 nm thick gold. Although coupling between the mode and the lossy surface plasmons associated with the lateral metal contacts can degrade performance (see Fig. 2), if the gap between the ridge and the contacts is kept large, any perturbative coupling effects are negligible in comparison with the case where the contacts are absent from the simulations. These results show that the degree of coupling between the mode and the surface plasmons under the lateral contacts is sensitive to the gap distance. Therefore, by assuming a large enough gap distance, these lateral contacts can safely be neglected in the remainder of these simulations for simplification. The mirror reflectivity was set at 0.3195 (from the effective index method using n_{eff}=3.6). This is shown to be a good approximate value for SI surface-plasmon waveguides as discussed in Sec. III.

The various parameters that determine the SI surface-plasmon waveguide performance are listed in Table I. Simulations to investigate the effect that these parameters have on the figure-of-merit (threshold gain) were carried out at the following set of frequencies: 2.0, 2.5, 3.0, and 3.5 THz. For our chosen active region thickness of 10 μm, 2.5 THz was approximately the lowest frequency for which a mode was still appreciably confined to the gain medium. A thicker active region is required at $f \lesssim$ 2.5 THz, which demands a proportionally longer molecular beam epitaxy (MBE) growth time. If free-carrier contributions to the loss and Re$\{\epsilon(\omega)\}$ were neglected, the results presented here would scale appro-

TABLE I. List of the SI surface-plasmon waveguide variables and their respective ranges for simulations carried out.

SI surface-plasmon waveguide parameters	
MBE growth parameters	
Plasma layer thickness	300–800 nm
Plasma layer doping n_{pl}	$(1.0–5.0) \times 10^{18}$ cm^{-3}
Active region thickness	10 μm (fixed)
Active region doping	2.0×10^{15} cm^{-3} (fixed)
Fabrication parameters	
Waveguide width	30–200 μm
Substrate thickness	10–250 μm
Side contact gap distance	5–50 μm

priately to the active region thickness to wavelength ratio. However, as will be discussed, the free-carrier effects play a significant role at lower frequencies, when the lasing frequency approaches the bulk plasma frequency of the free carriers in the active region. First, variations in the plasma layer thickness and doping were considered, since g_{th} is most sensitive to these parameters. Then, once an optimum plasma layer doping value was determined for each frequency, the waveguide width was varied. Different substrate thicknesses were considered last.

Doping levels were found for different frequencies such that g_{th} was minimized, both for cases of finite and infinite waveguide widths. An example of optimum doping is determined from a plot shown in Fig. 3, where g_{th} is plotted vs n_{pl} for various plasma thicknesses at 4 THz. Similar exercises were performed at other frequencies, with the results summarized in Table II. The optimum doping level is seen to decrease with a decreasing waveguide width from the optimum value given by one-dimensional analysis. The trend in optimal plasma layer parameters as the frequency decreases and/or waveguide width narrows is towards a lower doping value and a thicker layer. While both the lower doping value and thicker layer add to the waveguide loss α_w, the increase in confinement they provide makes these parameters more desirable as the waveguide width/height to wavelength ratio decreases. The confinement factor here, and for the cases that
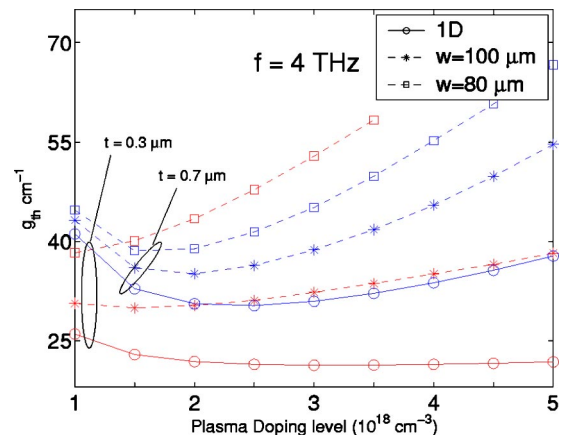

FIG. 3. (Color online) SI surface-plasmon waveguide simulation results at f=4.0 THz. Displayed are 1D and 2D threshold gain values vs plasma doping for plasma thicknesses of 0.3 and 0.7 μm; overlaid are 2D results for waveguide widths of 80 and 100 μm.

TABLE II. Optimal plasma layer doping values for the SI surface-plasmon waveguide. Values from one-dimensional calculations are presented in column two; values from two-dimensional calculations are presented in column three for waveguide widths specified in parentheses. Optimal plasma layer doping values are relatively independent of the choice of plasma layer thickness, which may be thin for wide waveguides and thicker for narrow waveguides.

	Optimal plasma doping levels	
Frequency (THz)	Infinite width n_{pl} ($\times 10^{18}$ cm^{-3})	Finite width n_{pl} ($\times 10^{18}$ cm^{-3}) (width in μm)
7.0	5.0	5.0 (50)
6.0	4.5	3.5 (60)
5.0	3.5	2.0 (70)
4.0	2.5	1.5 (100)
3.5	2.0	1.0 (125)
3.0	1.0	1.0 (150)
2.5	1.0	1.0 (200)

follow for the SI surface-plasmon waveguide, is seen to be the determining factor for these modes since it falls in the denominator of Eq. (1) and any changes in Γ below 0.5 substantially affects g_{th} more than similar changes in α.

Waveguide width effects, using optimal plasma doping levels taken from Table II, are displayed in Figs. 4–6 for frequencies between 2.5 and 3.5 THz. Overlaid in these figures are three sets of values for different plasma layer thicknesses that show the compromise that must be made in varying this parameter. The plasma layer thickness dramatically influences the confinement factor and overall loss. A thicker plasma layer will prevent "leakage" of the mode into the substrate and yield a higher confinement factor (up to $\Gamma \sim 0.5$), but this is accompanied by an increase in the loss as the mode overlaps a thicker lossy material. For one-
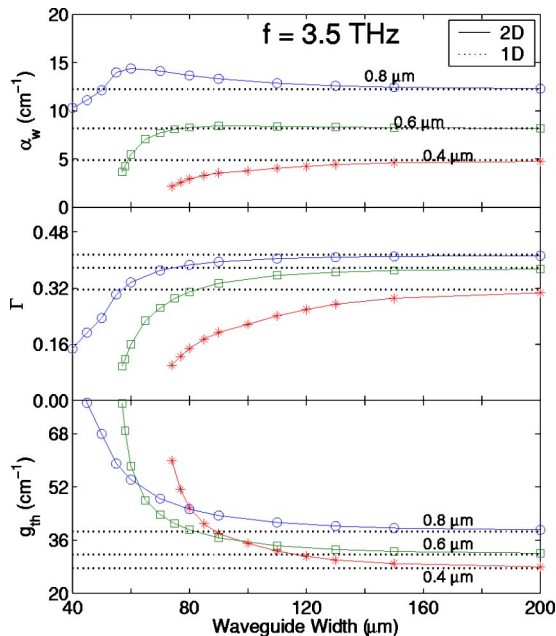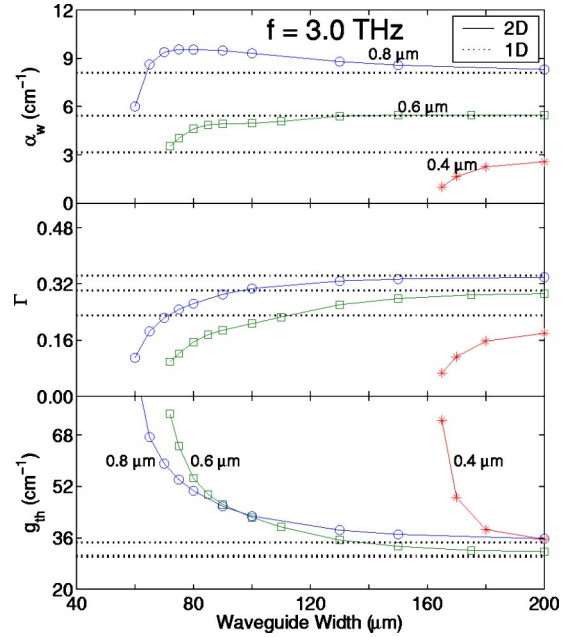

FIG. 5. (Color online) SI surface-plasmon waveguide simulation results at $f = 3.0$ THz. Displayed are 2D loss and confinement factors vs waveguide width for plasma thicknesses of 0.4, 0.6, and 0.8 μm at a plasma doping of 1.0×10^{18} cm^{-3}; 1D results are plotted to show convergence.

dimensional calculations above 3 THz, usually no compromise between loss and confinement is necessary as the thinnest plasma layer simulated, 300 nm, gives the lowest g_{th}. Below 3 THz, however, the confinement of the mode begins to suffer as the ratio of the active layer to the wavelength decreases. Considering just the infinite waveguide width case for the moment, the contribution from the plasma layer to the term α_w / Γ changes little as the frequency decreases. Here, the decrease in waveguide loss, due to the frequency decreas-

FIG. 4. (Color online) SI surface-plasmon waveguide simulation results at $f = 3.5$ THz. Displayed are 2D loss and confinement factors vs waveguide width for plasma thicknesses of 0.4, 0.6, and 0.8 μm at a plasma doping of 1.0×10^{18} cm^{-3}. 1D results are plotted to show convergence.
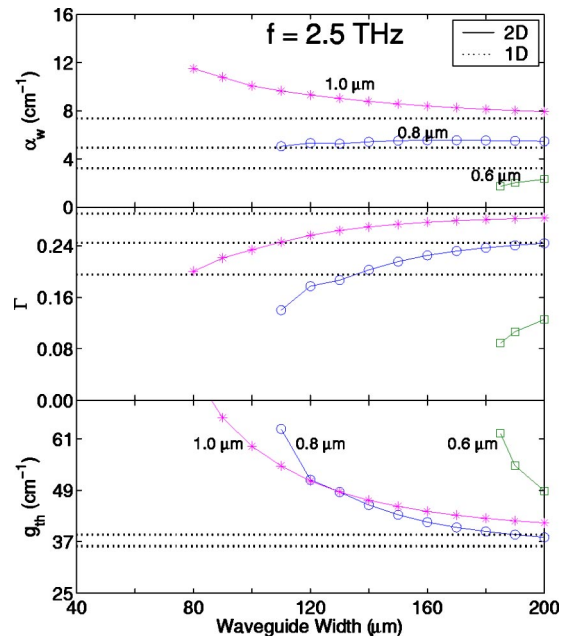

FIG. 6. (Color online) SI surface-plasmon waveguide simulation results at $f = 2.5$ THz. Displayed are 2D loss and confinement factors vs waveguide width for plasma thicknesses of 0.6, 0.8, and 1.0 μm at a plasma doping of 1.0×10^{18} cm^{-3}; 1D results are plotted to show convergence.
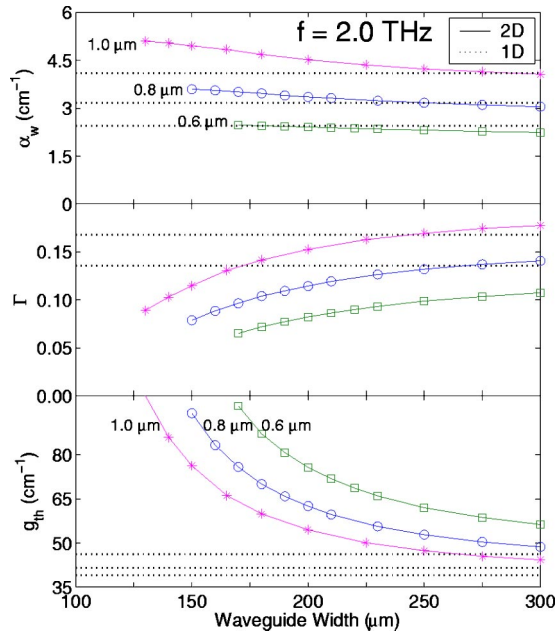
FIG. 7. (Color online) SI surface-plasmon waveguide simulation results at f=2.0 THz for a 15 μm thick active region on top of a 100 μm thick substrate. Displayed are 2D loss and confinement factors vs waveguide width for plasma thicknesses of 0.6, 0.8, and 1.0 μm at a plasma doping of 1.0 $\times 10^{18}$ cm^{-3}. 1D results are plotted to show convergence.
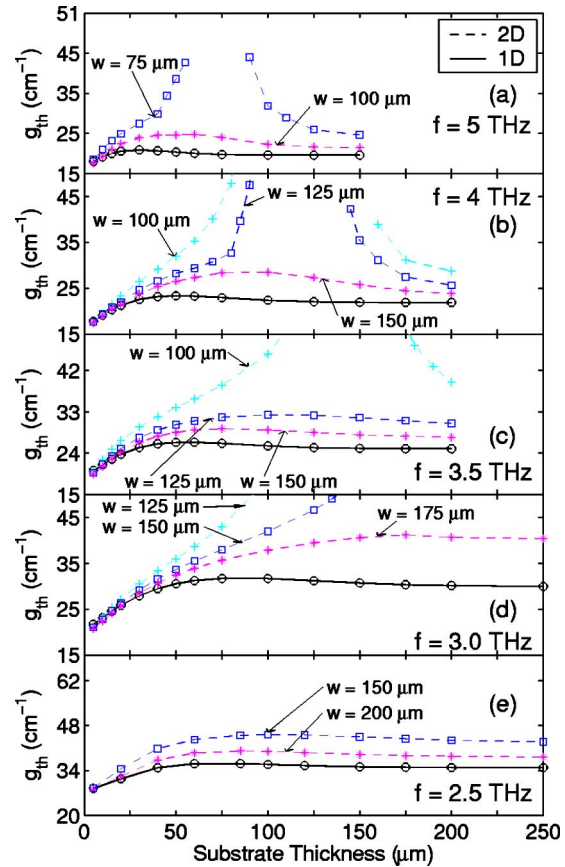

FIG. 8. (Color online) SI surface-plasmon waveguide simulation results of 1D and 2D loss and confinement factors vs substrate thickness. Waveguides with finite widths of various values are labeled. Plasma thickness of 0.3 μm were used in (a) and (b), 0.4 μm in (c) and (d), and 0.8 μm in (e); plasma doping levels were set at (a) 3×10^{18} cm^{-3} for f=5 THz, (b) 2×10^{18} cm^{-3} for f=4 THz, (c) 1.5×10^{18} cm^{-3} for f=3.5 THz, (d) 1×10^{18} cm^{-3} for f=3 THz, and (e) 1×10^{18} cm^{-3} for f=2.5 THz.

ing and moving further away from the bulk plasma frequency of the plasma layer, is nulled by the decrease in the confinement, due to the geometric effect where the wavelength increases relative to the active region thickness. However, as the facet loss α_m is nearly independent of the frequency, while the plasma layer contribution to the α_w/Γ term changes little vs frequency, the α_m/Γ term begins to blow up as the confinement degrades at lower frequencies. Therefore, while the plasma layer contribution to α_w decreases with the frequency, α_m does not, and for frequencies below 3 THz, thicker plasma layers are needed to prevent the term α_m/Γ from blowing up. If we now consider the effects that finite waveguide widths have on the confinement factor, we predict that thicker plasma layers will yield an even better figure-of-merit than that predicted by one-dimensional analysis below certain waveguide widths at all frequencies.

At frequencies below 2.5 THz, the reduction in Re$\{\epsilon(\omega)\}$ in the active region by the free carriers is significant enough such that the mode, in effect, becomes mainly confined to the SI substrate. Therefore, in order to optimize the waveguide design, the substrate should be thinned as much as possible. The confinement can also be increased by increasing the active region thickness. Figure 7 displays waveguide simulations carried out at 2.0 THz for a 15 μm thick active region on top of a 100 μm thick substrate.

The effect of substrate thickness is discussed next. Aside from the waveguide perspective, thin substrates offer thermal advantages during device operation. However, it is shown that in certain cases of narrow waveguide widths and thin plasma layers, thinning the substrate degrades the figure-of-merit. Figure 8 shows the effect of substrate thickness for different frequencies and waveguide widths. As the waveguide width decreases, the mode is pushed out of the active

region and couples more to the surface plasmon associated with the bottom metal contact. This effect where the bottom contact "pulls" the mode out of the active region increases with decreasing frequency. This is counter to an intuitive notion that thin substrates will simply push the "leaked" mode back into the active region and increase confinement. This latter effect does occur, but only for extremely thin substrates, when the wavelength in the semiconductor approaches the thickness of the substrate; and therefore the waveguide behaves more like a metal-metal waveguide. This situation is seen for some cases of low frequencies, where it can be advantageous to thin the waveguide in order to minimize the leak, as seen in Fig. 8(d). Increasing the confinement by using a thicker plasma layer will minimize the effect of coupling with the bottom metal contact for narrow waveguides.

B. Metal-metal waveguides

The metal-metal waveguides simulated for this paper consisted of an active region of varying thickness sandwiched between a 400 nm thick top metal contact and a metal substrate. The waveguide, like the SI surface-plasmon waveguide, is based on a double-sided surface-plasmon between the top and bottom metallic contacts. The dependence
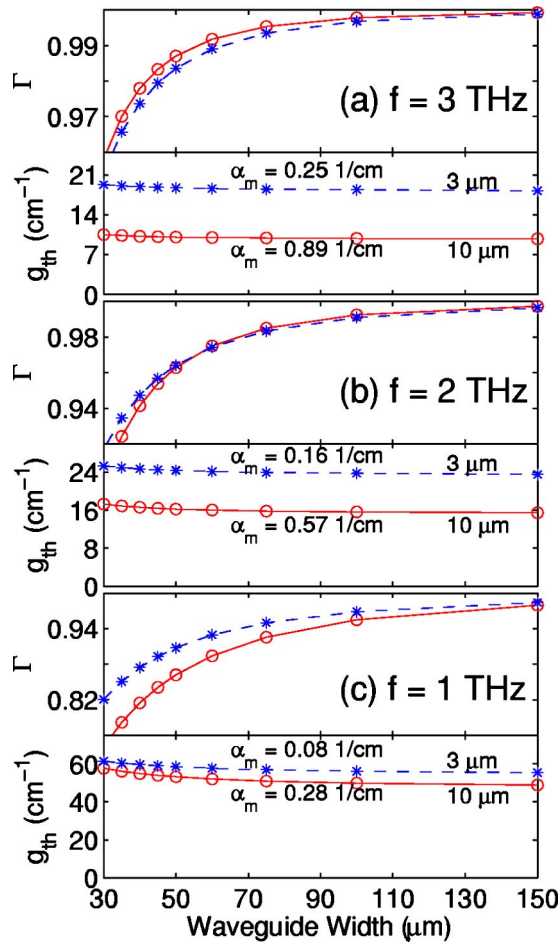
FIG. 9. (Color online) Metal-metal waveguide simulation results: 2D loss and confinement factors vs waveguide width for core thicknesses of 3 and 10 μm for (a) $f=3.0$ THz, (b) $f=2.0$ THz, and (c) $f=1.0$ THz.
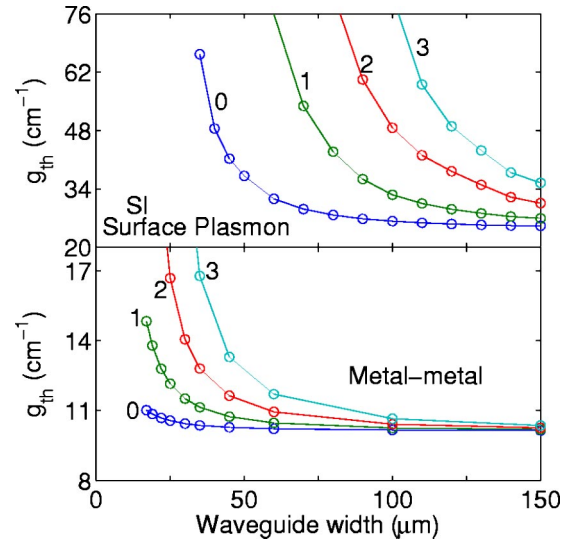

FIG. 10. (Color online) Threshold gain values for higher-order lateral modes vs waveguide width for (a) SI surface-plasmon waveguides and (b) metal-metal waveguides at 5 THz. The plasma layer in (a) is 0.5 μm thick and doped at 3×10^{18} cm^{-3}. Both structures are 10 μm thick.

of g_{th} on the metal-metal waveguide parameters of waveguide width and waveguide (active region) thickness are shown in Fig. 9 for frequencies of 1, 2, and 3 THz. Unlike the SI surface-plasmon waveguide, the mirror reflectivity depends on the frequency and waveguide geometry and therefore the values of α_m are taken from the calculations in Sec. III B. In the terahertz regime, mirror reflectivities for metal-metal waveguides are seen to be greater than those for SI surface-plasmon waveguides; therefore, the mirror coupling losses contribute less to the overall loss. In addition, since the confinement factors for all metal-metal waveguides are close to unity, the final figure-of-merit can be well approximated as simply the waveguide loss, α_w ($\approx g_{th}$).

The effect of varying the waveguide width at different frequencies is shown in Fig. 9, with each plot showing two different cases of active region thickness. The calculated waveguide loss increases as the active region thickness decreases, due to an increase in the relative modal overlap with the metal and lossy contact layers. For low frequencies, as the lasing frequency approaches the bulk plasma frequency of the active region (0.43 THz), the total waveguide loss becomes dominated by free-carrier loss associated with carriers in the active region itself. This is manifested by the decreasing sensitivity of g_{th} to the active region thickness at low frequencies, where losses associated with the metal contacts become less important.

Simulations were also carried out above 3 THz, where the metal-metal waveguide slightly improves on its already near unity confinement while exhibiting lower waveguide losses as the lasing frequency moves further away from the bulk plasma frequency of the active region. As such, waveguide loss above 3 THz is dominated more by losses associated with the surface plasmons at the metal contacts making the threshold gain more sensitive to the thickness of the active region. Nevertheless, the values of g_{th} shown in Fig. 9(a) represent the upper bounds in the frequency range of 3–7 THz.

In comparison with the SI surface-plasmon waveguide, g_{th} depends only weakly on the width of the waveguide and the metal-metal waveguide is capable of maintaining low threshold gain conditions for waveguide widths much less than the lasing wavelength in free space. One-dimensional simulations therefore provide adequate analysis for all but the narrowest of metal-metal waveguides. The higher confinement is partly due to the fact that the mode only is allowed to leak into the air on the sides rather than both the sides and the substrate, as in the case for the SI surface-plasmon waveguide. This allows the fabrication of very narrow waveguide ridges, which can be advantageous for reducing power dissipation and optimizing heat removal from the active region. In fact, we have achieved a record performance of cw operation up to 97 K from a 25 μm wide laser at 2.8 THz ($\lambda_0 \approx 107$ μm).[12] This laser device has the smallest width/wavelength ratio of any laser. However, as a result of its strong confinement, the metal-metal waveguide is capable of guiding far more lateral modes than the SI surface-plasmon waveguide at a given width. This is shown in Fig. 10, where g_{th} is plotted vs waveguide width for several higher-order lateral modes. In our experiments, we have observed only multilongitudinal modes from the SI surface-plasmon laser devices, but frequently observe multilateral modes (as well as longitudinal ones) from the metal-metal waveguide lasers. In this respect, the SI surface-plasmon

waveguide exhibits higher mode selectivity for achieving single-lateral-mode laser operation, and is more conducive to the fabrication of wide laser ridges for high output power.

C. Waveguide discussion

In summary, two-dimensional results were used to find the optimum doping and thickness for plasma layers accounting for the finite widths of SI surface-plasmon ridge waveguides. It was found that the waveguide behavior deviates substantially from that predicted by a one-dimensional model for ridge widths narrower than five to six times the radiation wavelength in the semiconductor. This occurs as the mode is squeezed out of the active region into the substrate and reduces Γ, which, when Γ is below 0.5, g_{th} is quite sensitive to. While some improvements may be possible in the design of SI surface-plasmon waveguides, such as graded doping of the plasma layer,[13] the waveguide displays larger threshold gains in comparison to the metal-metal waveguide for all the frequencies investigated (1–7 THz). The main obstacle in obtaining low threshold gains for the SI surface-plasmon waveguide is its poor ability to confine the mode, which results in confinement factor values of $\Gamma = 0.1$–0.5. In particular, the confinement drops at lower frequencies, both due to a geometric effect where the wavelength increases relative to the active region thickness, and due to the $1 - \omega_p^2/\omega^2$ reduction of the dielectric constant in the lightly doped active region. As a result of this reduction in $\text{Re}\{\epsilon(\omega)\}$ by the free carriers, the mode extends further into the substrate where the dielectric constant is higher, unless confined by excessive thinning of the substrate. The metal-metal waveguide, on the other hand, has a confinement factor close to unity, and yields lower threshold gains across the frequency range investigated (1–7 THz), with little dependence on the waveguide width. However, while the metal-metal waveguide outperforms the SI surface-plasmon waveguide in terms of waveguiding, it underperforms in terms of its ability to couple power out. This issue is discussed in the following section.

III. RESONATOR ANALYSIS

The resonator of a laser includes both the waveguide and mirrors. This section focuses on mirror reflectivities and the radiation pattern of the laser. We consider ridge waveguides where the mirrors for both waveguides are simply constructed by cleaving the waveguides; the resulting facets, due to the orientation of the crystalline lattice, are approximately perfect planes.

Because of memory limitations, in the metal-metal resonator simulations, all materials were made lossless and the metals were replaced with perfect electrical conductor (PEC) boundary conditions, that is, the tangential component of $\mathbf{E} \equiv \mathbf{0}$. The inherent nature of the SI surface-plasmon mode prevents the use of such a lossless approximation. Therefore, an appropriate gain was included in the active region to balance losses in the plasma layer and prevent decay of the input eigenmode. Unfortunately, due to the severe aspect ratio in the SI surface-plasmon waveguide geometry and the memory requirements in full-wave three-dimensional nu-

merical processing, no simulations could be performed in three dimensions for the SI surface-plasmon waveguide.

The simplest method to determine the facet reflectivity is to divide the reflected power P_r by the input power P_{in}. However, in two-dimensional simulations, for waveguides with more than one propagating mode, the reflected power is usually carried by more than one mode of the waveguide due to the excitation of higher-order modes at the facet. Higher-order modes with an imaginary propagation constant are evanescent and do not carry power; however, in three dimensions, evanescent modes, due to the finite width of the waveguide, are leaky and do carry power away laterally. For our threshold gain condition in Eq. (1), the relevant parameter is the reflection coefficient into the mode of interest and excludes any reflections into higher order modes; therefore, this method of calculating the power reflection is not always adequate. Instead, the standing-wave ratio (SWR) method is used to obtain a more accurate value for the reflectivity into a specific mode. We assume that the total field in the waveguide is composed of a forward propagating fundamental mode $\mathbf{h}_0(x,y)e^{i\beta_0 z}$, the mode of interest, and backward propagating modes of all orders due to excitation at the facet,

$$\mathbf{H}(x,y,z) = \mathbf{h}_0(x,y)e^{i\beta_0 z} + \sum_i r_i \mathbf{h}_i(x,y)e^{-i\beta_i z}, \qquad (3)$$

where the r_is are the amplitude reflection coefficients into each respective mode. The SWR is defined by the ratio of the maximum to minimum value of the standing wave

$$\text{SWR} = \frac{|\langle \mathbf{h}_0(x,y)|\mathbf{H}(x,y,z)\rangle|_{\max}}{|\langle \mathbf{h}_0(x,y)|\mathbf{H}(x,y,z)\rangle|_{\min}} = \frac{1 + |r_0|}{1 - |r_0|}, \qquad (4)$$

where the inner product $\langle \mathbf{h}_0|\mathbf{H}\rangle \equiv \int\int \mathbf{h}_0^* \cdot \mathbf{H} dx\, dy$. The calculation of the facet reflectivity therefore only needs the maximum and minimum values of the standing wave defined in Eq. 4 to obtain a value of

$$R = |r_0|^2 = \left(\frac{\text{SWR} - 1}{\text{SWR} + 1}\right)^2. \qquad (5)$$

A. SI surface-plasmon resonators

As discussed in Sec. II, previous analyses of SI surface-plasmon waveguides used the effective index method in calculating the mirror coupling loss. For a GaAs/Air interface, where $n_{\text{GaAs}} \approx 3.6$, this gives a mirror reflectivity of $R \approx 0.32$. Selected frequencies were simulated for the SI surface-plasmon waveguide and the results are shown in Table III. The thickness of the active region is 10 μm for all the frequencies simulated. Waveguide parameters were kept constant except for the plasma doping level, which was changed to correspond to the optimum (minimized g_{th}) level for each frequency. As seen, numerical results for all frequencies tested are sufficiently close to values given by the effective index method to reaffirm its validity in calculating mirror reflectivities for the SI surface-plasmon waveguide. Far-field radiation patterns were also calculated at frequencies of 2, 3, and 5 THz for the SI surface-plasmon waveguide. No severe diffraction effects are seen and the far-field

TABLE III. SI surface-plasmon facet reflectivities for 2–6 THz. All of the structures simulated have the following geometry: 0.4 μm top metal contact, 10 μm active region (doped at 2×10^{15} cm^{-3}), 0.5 μm plasma layer (doping listed), on a 100 μm substrate with a bottom metal coating. Calculations using the effective index method ($n_{eff} = \beta/k_0$) are listed for comparison. These simulations neglect any contributions to the refractive index due to phonons.

| | SI surface-plasmon waveguide facet reflectivities Reflectivity (%) | | |
Frequency (THz)	Simulated	n_{eff} Method	Plasma layer doping ($\times 10^{18}$ cm^{-3})
2.0	28.95	31.99	1.0
2.5	32.71	32.03	1.0
3.0	33.26	32.08	1.0
4.0	32.08	32.17	2.0
5.0	31.24	32.26	3.0
6.0	30.21	32.35	4.5

pattern is similar to that predicted by Fraunhofer diffraction from a uniformly excited aperture in an infinite PEC ground plane.

B. Metal-metal resonators

Waveguide apertures for metal-metal structures are much smaller than the lasing wavelength in free space and thus previous approximations used in optical and midinfrared waveguides for reflection and transmission calculations are no longer valid. These failures mainly come about because previous theories assume that incident and transmitted waves are plane waves with infinite extent. In addition, they assume fields free of coupling effects with the aperture's boundary, where for subwavelength apertures this effect becomes nonnegligible.

Figure 11 displays two-dimensional results of metal-metal facet reflectivities vs frequency for different values of the active region thickness (waveguide height). The effective index method fails to describe the higher facet reflectivities that occur in the terahertz regime (1–10 THz). The increase in reflectivity, or decrease in transmission, can be understood in the context of antenna theory, where power radiated from
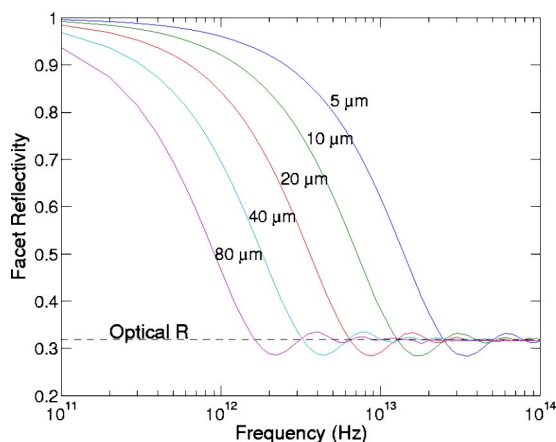
FIG. 11. (Color online) Two-dimensional (waveguide width is infinite) metal-metal waveguide facet reflectivities vs frequency for five different waveguide thicknesses 5, 10, 20, 40, and 80 μm.
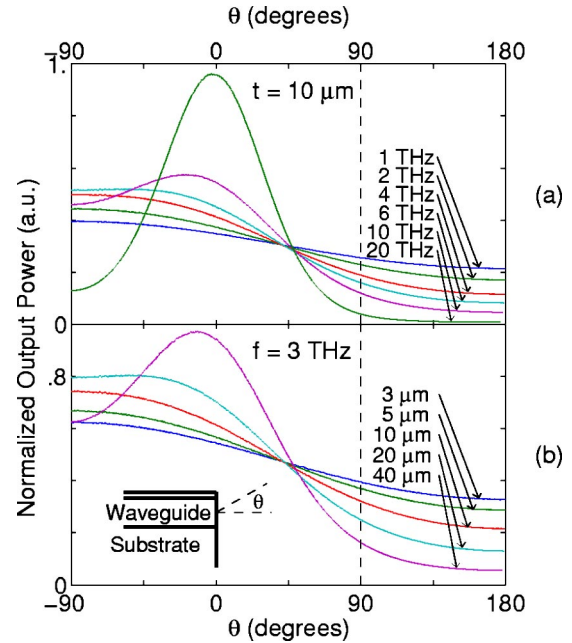
FIG. 12. (Color online) Normalized two-dimensional (infinite waveguide width) power radiation patterns for metal-metal waveguides. (a) Sets of power radiation patterns at different frequencies for a waveguide thickness of 10 μm. (b) Sets of power radiation patterns at different waveguide thicknesses for $f=3$ THz.

a subwavelength aperture is approximately proportional to the area of the aperture. The oscillatory behavior as the reflectivity converges to the optical reflection value suggests an enhanced transmission of light at frequencies where $R < 0.32$ in comparison with plane-wave transmission. The most pronounced minima in R in fact occur when the waveguide thicknesses are approximately half of the free-space wavelengths. An analogy can be made in this case with the ideal finite-length dipole antenna, in which analytical results show local maxima and minima in radiation resistance for dipole lengths at approximately integer multiples of half wavelengths.[10] In fact, if we consider the SI surface-plasmon resonator approximated as a metal-metal waveguide with a thickness of 110 μm (10 μm active region plus 100 μm substrate), then from Fig. 11 we see that indeed the reflection values should be close to the optical reflection. In addition, the changes in the simulated reflection values in Table III follow the same oscillatory behavior as metal-metal waveguides simulated with other thicknesses right before their reflection values diverge from the optical reflection value.

Diffraction of the fields at the aperture also clearly diverge from results predicted by Fraunhofer diffraction from a uniformly excited aperture in an infinite PEC ground plane, shown in Fig. 12 where considerable power is delivered both down the side of the substrate ($\theta < -45°$) and back above the top metal contact ($\theta > 90°$). Figure 12(a) displays power directivity "beam" patterns at varying frequencies for a fixed thickness 10 μm thick metal-metal waveguide and Fig. 12(b) displays power directivity beam patterns for varying thicknesses of the metal-metal waveguide at a frequency of 3 THz. Except for the effect of the conductive substrate, this scenario is similar to that of the radiation from a parallel
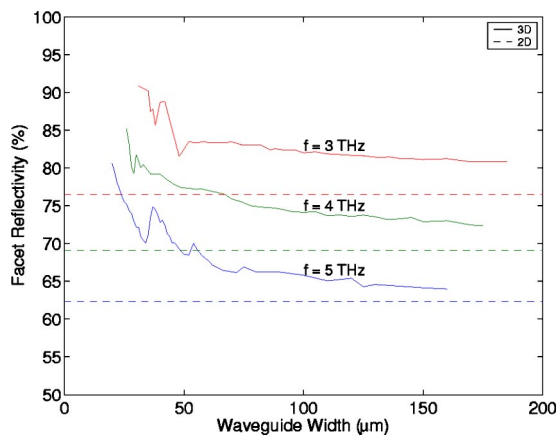
FIG. 13. (Color online) Three-dimensional metal-metal waveguide facet reflectivities vs waveguide width for $f=3$, 4, and 5 THz with a waveguide thickness set at 10 μm; dashed lines give the two-dimensional values to show convergence.

plate waveguide. Due to severe diffraction and aperture boundary effects, the radiation is highly divergent with a significant fraction radiated up and behind ($\theta > 90°$) the waveguide with respect to the facet. Without a full metal plane at the aperture to block radiation at $|\theta| > 90°$, reradiation of the field in the reverse direction is possible from Huygens' principle. Only a fraction of the output power is therefore radiated within a small enough angle to be collected by appropriate optics. Because of this beam divergence, the measured (uncorrected) power level of ~1 mW in Ref. 5 is likely only a small fraction of the total output power of the laser device.

Just as decreasing the waveguide height increases the facet reflectivity, decreasing the waveguide width also increases the facet reflectivity, as shown in Fig. 13. Figure 13 displays three-dimensional results of metal-metal facet reflectivities for waveguides with finite widths. The increase in reflectivity that is observed as the waveguide width decreases can be explained by the decrease in the area of the waveguide aperture.

C. Resonator discussion

Two- and three-dimensional simulation results for SI surface-plasmon and metal-metal resonators in the THz regime have been presented. The effective index method is shown to be valid in the THz regime for calculating facet reflectivities for SI surface-plasmon resonators. The larger effective area that the mode covers in this case (both in the active region and a substantial part of the substrate) helps explain its adherence to the effective index method, while the

subwavelength metal-metal waveguide fails to. Radiation patterns for SI surface-plasmon waveguides are similar to that predicted by Fraunhofer diffraction from a uniformly excited aperture in an infinite PEC ground plane. Metal-metal resonators, on the other hand, are more appropriately described by microwave models as the facet reflectivity increases dramatically and the directivity of the output power decreases since the waveguide aperture is much smaller than the free-space wavelength.

With the tight mode confinement, the metal-metal waveguide has a clear advantage over the SI surface-plasmon waveguide to obtain a reduced lasing threshold. However, the trade off is a poor out coupling of power from the cavity and a highly divergent beam pattern. The high facet reflectivity results in a small value of the mirror loss α_m (typically ~1 cm^{-1}) compared to the waveguide loss (typically 10–20 cm^{-1}). This results in a small value of the out-coupling factor $\alpha_m/(\alpha_w + \alpha_m)$, which appears in the expression for the optical slope efficiency of a laser. In order to increase the out-coupling efficiency and improve the radiation pattern of the metal-metal waveguide lasers, mode matching structures including horn antennas and horn-to-waveguide mode converters can be used, just like the case in all the millimeter-wave sources and detectors.[14]

[1]R. Köhler *et al.*, Nature (London) **417**, 156 (2002).
[2]M. Rochat, L. Ajili, H. Willenberg, J. Faist, H. Beere, G. Davies, E. Linfield, and D. Ritchie, Appl. Phys. Lett. **81**, 1381 (2002).
[3]B. S. Williams, H. Callebaut, S. Kumar, Q. Hu, and J. L. Reno, Appl. Phys. Lett. **82**, 1015 (2003).
[4]B. S. Williams, S. Kumar, H. Callebaut, Q. Hu, and J. L. Reno, Appl. Phys. Lett. **83**, 2124 (2003).
[5]S. Kumar, B. S. Williams, S. Kohen, Q. Hu, and J. L. Reno, Appl. Phys. Lett. **84**, 2494 (2004).
[6]All two- and three-dimensional simulations were carried out in FEMLAB3.0, a finite-element based partial differential equation software solver.
[7]S. L. Chuang, *Physics of Optoelectronic Devices*, Wiley Series in Pure and Applied Optics, 1st ed. (Wiley, New York, 1995).
[8]S. Barbieri *et al.*, IEEE Tenth International Conference on Terahertz Electronics Proceedings (IEEE, Piscataway, NJ, 2002), pp. 105–108.
[9]J. Faist, F. Capasso, D. L. Sivco, C. Sirtori, A. L. Hutchinson, and A. Y. Cho, Science **264**, 553 (1994).
[10]C. A. Balanis, *Antenna Theory: Analysis and Design*, 2nd ed. (Wiley, New York, 1997).
[11]T. Ando, A. B. Fowler, and F. Stern, Rev. Mod. Phys. **54**, 437 (1982).
[12]Q. Hu, B. S. Williams, S. Kumar, H. Callebaut, S. Kohen, and J. L. Reno, Semicond. Sci. Technol. (to be published).
[13]D. Indjin, Z. Ikonić, P. Harrison, and R. W. Kelsall, J. Appl. Phys. **94**, 3249 (2003).
[14]P. H. Siegel, IEEE Trans. Microwave Theory Tech. **50**, 910 (2002).